PERGAMON

Journal of Structural Geology 22 (2000) 411–427

JOURNAL OF STRUCTURAL GEOLOGY

www.elsevier.nl/locate/jstrugeo

Micromechanics of shear rupture and the control of normal stress

Christopher A. J. Wibberley[a,*], Jean-Pierre Petit[b], Thierry Rives[c]

[a]*Department of Geology and Mineralogy, Division of Earth and Planetary Sciences, Graduate School of Science, Kyoto University, Kitashirukawa-oiwake cho, Kyoto 606-8502, Japan*

[b]*Laboratoire de Géophysique et Tectonique, c.060, Université Montpellier II, Place E. Bataillon, 34095 Montpellier, France*

[c]*Elf EP, Avenue Larribau, 64018Pau, France*

Received 10 March 1999; accepted 12 October 1999

Abstract

Conjugate microfault zones and distributed tensile microcracks were observed in low porosity sandstone samples deformed by shear box rupture at different normal stresses. Statistical data collected from scanning electron microscopic mapping show that tensile microcracks and microfaults are more frequent in the higher normal stress cases. The average thickness of the cataclastic microfault zones increases proportionally to rupture normal stress. The density of tensile microcracks increases locally in microfault relay and intersection zones where their formation is an important mode of microfault zone cataclasis. Concentration of longer en échelon tensile microcracks occurs in process zones ahead of the microfault tips, connected by cross-cracks in an incipient breakdown zone to further propagate the fault. Fracture densities are much lower in calcite cement grains whose compliancy serves to arrest microfault growth temporarily, yet also aid intragranular microcracking in adjacent stiff grains and at grain boundaries. Tensile microcrack and microfault average dips from the sample rupture surface increase with rupture normal stress, with conjugate microfault orientation variability at higher normal stresses aiding their connectivity. Results of this investigation demonstrate how the fracture porosity and connectivity around rupture zones increase dramatically at increased rupture normal stress, impacting on hydrodynamic properties of rupture zones.

1. Introduction

Understanding the rupture of initially intact rock is a basic aim of experimental rock deformation in the brittle field. However, in the development of rock mechanics, understanding shear fracture initiation and propagation at grain and crack scales has been relatively slow with respect to other aspects such as overall stress–strain relationships and the evolution of petrophysical properties under various loading conditions. This slow development is linked in particular to scarce studies specifically based on scanning electron microscope (SEM) observations aiming to study fault initiation over a significant surface within the samples at various steps of the loading history. As noted by Paterson (1978), slow progress was partly due to "the inhibiting idea that, since the field of view is very limited at the high magnification needed for seeing small cracks, it is necessary to know, a priori, the localisation of highly localised sites of cracking as envisaged in the simple Griffith model". The proposition that a shear fracture could not propagate in its own plane (Brace and Bombolakis, 1963) led to the suggestion that faults initiated by chance linkage of some of these distributed pre-existing microcracks. Indeed, it has been found that rupture of initially intact rock during triaxial deformation experiments is preceded mainly by microcracks which form during the dilatant phase of loading (e.g. Brace et al., 1966; Scholz, 1968; Peng and Johnson, 1972; Hallbauer et al., 1973). These microcracks were shown to be mainly load parallel tensile

* Corresponding author.

E-mail address: cwibber@ip.media.kyoto-u.ac.jp (C.A.J. Wibberley).

0191-8141/00/$ - see front matter
PII: S0191-8141(99)00158-3

microfractures of various origins, rather than oblique cracks (Tapponnier and Brace, 1976; Horii and Nemat-Nasser, 1985). More recently, works using the precise location of acoustic emission events (AE) (Lockner et al., 1991, 1992; Reches and Lockner, 1994) related to tensile microcrack generation throughout the loading cycle have mapped microcrack formation prior to failure. They show that although in an initial step microcracking occurs randomly, the fault soon initiates by chance interaction of cracks even at relatively low average crack density. The fault propagates by forming a high density of new microcracks controlled by a stress concentration at the tip of the proto-microfault in a process zone. In this zone, the generation of dense microcracking leads to yielding of the rock and to fault propagation. However, works aimed at describing the precise mechanisms of crack coalescence and cataclasis in the proto-microfault and microfault development remained scarce (Dunn et al., 1973; Gallagher et al., 1974).

Interpretations from AE data are in agreement with observations on fracture mechanics experiments in PMMA (Plexiglas), showing en échelon tensile microcracks ahead of imposed oblique faults (slots) at low angles to the overall direction of maximum compression (Petit and Barquins, 1988). They are also consistent with field, hand specimen and thin section observations on fault tip zones which also demonstrate the common occurrence of en échelon tensile fracture arrays adjacent to fault tips (e.g. Etchecopar et al., 1986; Petit and Barquins, 1988; McGrath and Davison, 1995; Granier, 1985). This association also suggests that it is the linking of such en échelon cracks (by some not yet fully understood mechanism) that causes fault propagation. The major role of the moving, small-scale fault tip in triaxial experiments was confirmed by Moore and Lockner (1995) on the basis of statistics on crack densities and orientation. Additionally, microfracture density peaks have been shown to exist adjacent to some small-scale natural faults (Vermilye and Scholz, 1998), possibly related to process zone deformation as the fault tip, or a later rupture event, propagates. In spite of these works, the relationship between tensile microcracking, proto-microfault development and fault localisation during continued deformation remains unclear, and the mechanisms of microfault interactions practically unstudied. This is mostly due to the lack of direct imaging of such structures during different stages of their evolution.

In this paper, we present SEM images of initially intact low porosity sandstone samples deformed by shear rupture in shear box experiments at a range of normal stresses. The SEM images are of the montage type, allowing suitably good coverage of a representative area of specimen, enabling us to map microcrack/microfault interactions. Firstly, we present relatively large SEM montages of post-failure shear ruptured

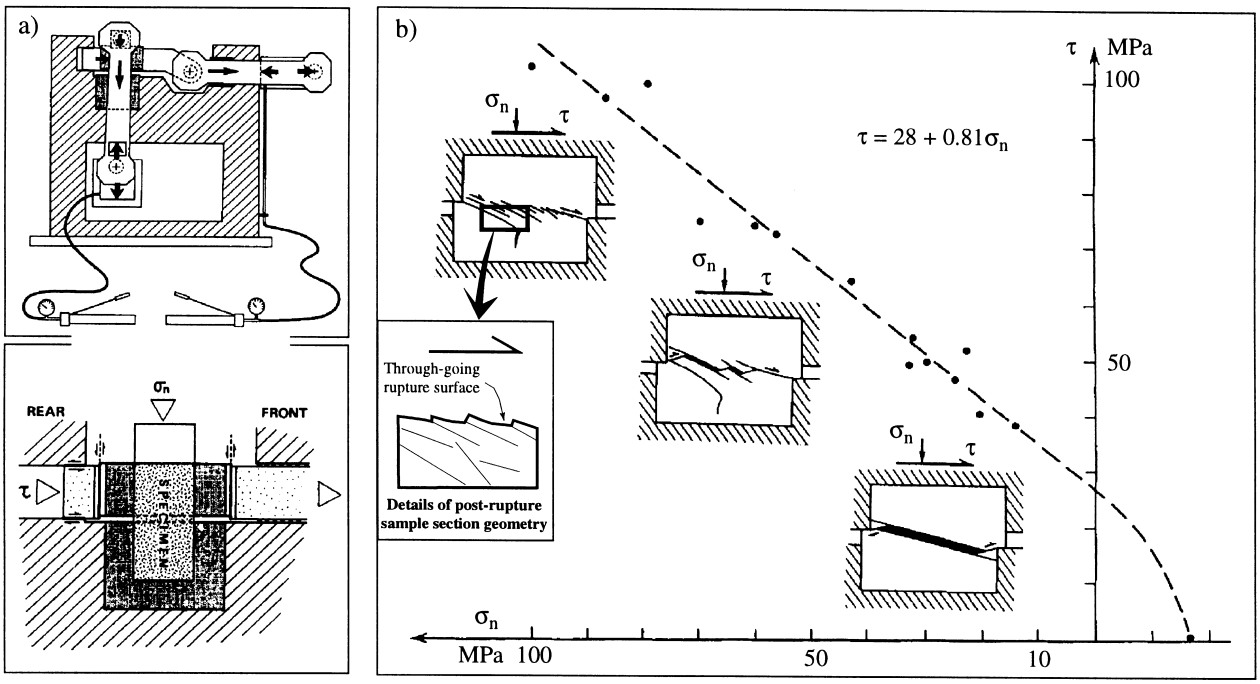

Fig. 1. (a) Experimental apparatus used to shear rupture the samples (from Petit, 1988). (b) Shear stress (τ) vs. normal stress (σ_n) at shear failure for the Lodève sandstone samples, with schematic appearance of rupture surfaces in hand specimen, as a function of normal stress during shear rupture (from Petit, 1988).

Table 1
Fracture frequency statistics for the samples ruptured at 15, 23, 60 and 87 MPa

Scan line		Scan line length (mm)	No. normal microcracks per mm	No. calcite g.b. microcracks per mm[a]	No. other g.b. microcracks per mm[a]	Total No. microcracks per mm	No. microfaults per mm	Total width of microfaults (mm) per mm
15 MPa	0 mm	20.4	0.196	0	0	0.196	0	0
	1 mm	11.6	0.259	0	0	0.259	0	0
	4 mm	8.2	0.122	0	0	0.122	0	0
Average			0.192	0	0	0.192	0	0
23 MPa	0 mm	36.5	0.822	0.027	0.027	0.877	0.11	0.005269
	1 mm	36.5	0.247	0	0	0.247	0.082	0.0036401
	4 mm	36.5	0.055	0	0	0.055	0.055	0.001832
Average			0.375	0.009	0.009	0.393	0.0823	0.003581
60 MPa	0 mm	11.2	7.589	1.161	0.357	9.107	0.536	0.01618
	1 mm	11.2	6.696	0.893	0.268	7.857	0.446	0.02092
	4 mm	11.2	8.393	1.071	0.714	10.179	0.446	0.01251
Average			7.559	1.0417	0.446	9.0477	0.476	0.01654
87 MPa	0 mm	23.3	3.223	0.344	0	3.567	0.43	0.02557
	1 mm	30.1	2.33	0.2	0	2.527	0.399	0.03703
	4 mm	27.1	2.844	0.185	0	3.029	0.369	0.01722
Average			2.799	0.243	0	3.041	0.399	0.03018

[a] g.b. denotes grain boundary.

samples systematically for cases of deformation at different normal stresses. Secondly, we focus on the details of microcrack/microfault relationships to make deductions about their relative geneses and roles in the generation of cataclastic material and controls on hydrodynamic properties. By comparing the different samples, the role of normal stress on rupture and resulting wall rock fracturing is also assessed, and the relevance of these findings on likely wall rock and rupture zone permeabilities and hydraulic storativities is considered.

2. Background

2.1. Material and experimental procedure

Cuboid samples, 200 mm × 100 mm × 100 mm, of early Permian very low porosity Lodève sandstone were deformed in a shear box by shear rupture perpendicular to the long axis of the sample (Petit, 1988). The Lodève sandstone is medium grained, being composed of quartz, albite and potassium feldspars, and is very well cemented by calcite. This calcite cementation gives the sandstone the extremely low porosity, as deduced from SEM observations. The experimental device is illustrated in Fig. 1(a). Experimental shear rupture was undertaken in dry conditions at room temperature, and under a different imposed constant normal stress for each experiment (see Fig. 1b). For each experiment, the applied shear stress was increased in steps of 1 MPa until failure occurred. The measured rupture shear stress at the various experimental normal stresses defined a Mohr failure envelope that follows the Mohr–Coulomb failure criterion (Fig. 1b).

2.2. Hand specimen observations

The macrostructural response to shear rupture deformation at different normal stresses has been analysed by Petit (1988) so that only a brief summary is needed here. Fig. 1(b) shows a hand specimen characterisation of the resulting rupture surfaces for examples of low, moderate and high normal-stress shear rupture. At the lowest normal stress (15 MPa) rupture failure was brutal (instantaneous to the naked eye), with a single low-angle rupture surface (10° to the principal shear plane) opening to become a dilatant pull-apart. This surface is linked to the sample boundaries by 'edge-effect' shear fractures, which are related to stress concentrations at the leading edges of the shear box walls. At moderate normal stress (60 MPa) many Riedel fractures, at 30–45° to the principal shear plane (and not necessarily connected to the sample edges) defined a shear zone prior to rupture, with the creation of much less dilational pull-apart space. In this case, the rupture failure was more gradual, presumably reflecting a lower rate of stress drop after peak shear stress. This trend continued to the highest normal stress example (87 MPa) with even more Riedel fractures appearing to form obliquely to the principal shear plane. The relatively slow linkage of these oblique Riedel fractures to form the through-going rupture surface suggests that many of these fractures accommodated shear displacements at least during the post-peak stress phase. At increasing normal stress, gener-

ally, a higher frequency of Riedel fractures intersecting the rupture surface was observed.

2.3. Methodology of present study

The aim of the work presented here is to investigate the fracture networks within the samples, using SEM techniques. Back-scattered SEM imaging was used because of its practical nature for micromapping, with different grey levels representing the different minerals (see caption to Fig. 3a) and black representing sample resin where no rock material is present (i.e. sample edges or fracture space). This makes imaging of even the smallest fractures easy (down to a fracture length of ~10 μm). Polished thin sections (35–40 mm in length) were made of the lower sheared blocks (see inset in Fig. 1b), cut perpendicular to the failure surface, parallel to the shear direction, and away from the sample edges. Fractures are classified as tensile microcracks (either intragranular or transgranular) referred to as 'normal microcracks' in Table 1, grain-boundary cracks [either involving calcite grains at one or both crack edges ('calcite grain-boundary cracks') or not involving calcite grains ('other grain-boundary cracks')], and microfaults. Microfaults are fractured surfaces along which some shear displacement has occurred. The microfaults often contain zones of grain fragments, or cataclastic material. Microfault senses of shear are deduced either from grain offsets, microclast rotations or inferred from pull-apart geometries or the relationship with tensile branch cracks (Petit and Barquins, 1990).

The first part of our data analysis focuses on examples of deformation at normal stresses of 15 MPa, 23 MPa, 60 MPa and 87 MPa. Statistical data on fracture densities and orientations are presented to characterise quantitatively the resulting damage as a function of normal stress. These statistical data were collected from scan lines parallel to the overall sample rupture surface. Scan line lengths (see Table 1) usually cover most or all of the polished thin section, with the exception of the 60 MPa case which had the highest frequency. In this case 30% of the thin section length was enough to obtain meaningful statistics. Three scan lines were used for each sample: the first placed as close to the general rupture surface on the sample image as was feasibly possible ('0 mm'), the second and third scan lines being at 1 and 4 mm, respectively from the first (measuring perpendicularly away from the rupture surface). For each scan line, individual microfault zone thicknesses were measured. The sum of these thicknesses was divided by the scan line length to obtain the total width of fault zones (in mm) per millimetre. This statistic is a one-dimensional equivalent of the proportion of total volume of the fault zones to total rock volume.

In the second part of our data analysis, the example of rupture at 60 MPa normal stress is then investigated in further detail. Enlargements are presented of some of the most interesting areas, in order to assess the role of tensile microcracking in microfault propagation, branching and cataclasite generation.

3. Data: influence of normal stress on fracture network properties

3.1. Samples deformed at low normal stress

A sample deformed at 15 MPa shows little wall rock deformation away from the rupture surface, with extremely low fracture frequencies (Table 1). Features of interest are restricted to a few tensile fractures of very low angles with respect to the rupture surface. A very small amount of wall rock damage occurred during rupture at low normal stress.

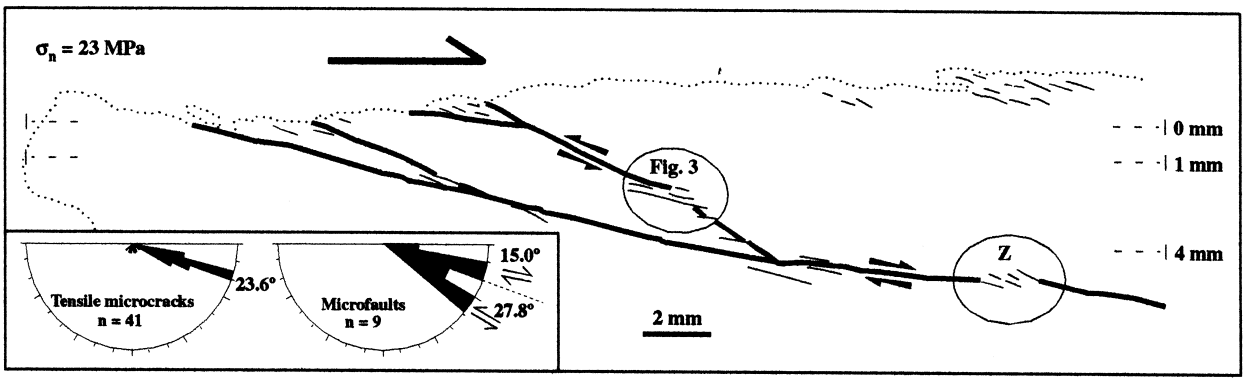

Fig. 2. Interpretative tracing of microfractures and microfaults from a backscattered scanning electron micrograph of a sample after shear rupture at 23 MPa. The upper surface of this image is the rupture surface. Rose diagrams give the combined orientation statistics as measured on the scan lines marked 0 mm, 1 mm and 4 mm. The scan line markings indicate the full length of the scan lines.

3.2. Samples deformed at moderately low normal stress

An example of rupture at 23 MPa (Fig. 2) shows more wall rock fracturing than the sample deformed at 15 MPa (Table 1). Microfaults here are still at a relatively low angle with respect to the rupture surface, but extend further into the wall rock than in the lowest normal stress case. Two groups of microfaults are present: synthetic microfaults form very low angles to the overall rupture surface (average 15.0°), whereas antithetic microfaults form higher angles with the overall rupture surface (average 27.8°). The tensile microcracks generally bisect these microfault orientations (average 23.6°). The density of tensile microcracks decreases exponentially away from the rupture surface (Table 1).

The microfaults are discontinuous and linked in places by zones of transgranular tensile microcrack concentration (e.g. Fig. 2, Zone Z and Fig. 3), where some cataclasis by tensile failure has occurred (Fig. 3). These zones have the same microfault/tensile microcrack relationship as branch cracks at fault tip zones, and illustrate how individual fault segments may link up in directions parallel to displacement (Fig. 2).

3.3. Samples deformed at moderate normal stress

Figs. 4 and 5 represent a sample deformed at a normal stress of 60 MPa. Wall rock fracturing is clearly much more intense than in the previous examples, and a marked orientation grouping of the microfaults is visible. These microfaults have a much greater penetration into the wall rock away from the rupture surface, as illustrated by the frequency data in Table 1. Figs. 4 and 5 show how the connectivity of the microfaults is assisted by the higher angle between synthetic and antithetic microfaults (~45°) than in the 23 MPa case. Note that the rose diagram depicting microfault orientations in Fig. 4 does not illustrate this conjugate relationship as well as the drawing in Fig. 5. This is because the synthetic faults are nearly parallel to the scan lines hence reducing the probability of intersection so that these microfaults have been grossly undersampled. This rose diagram is further complicated by a marked variation in orientation of antithetic faults in

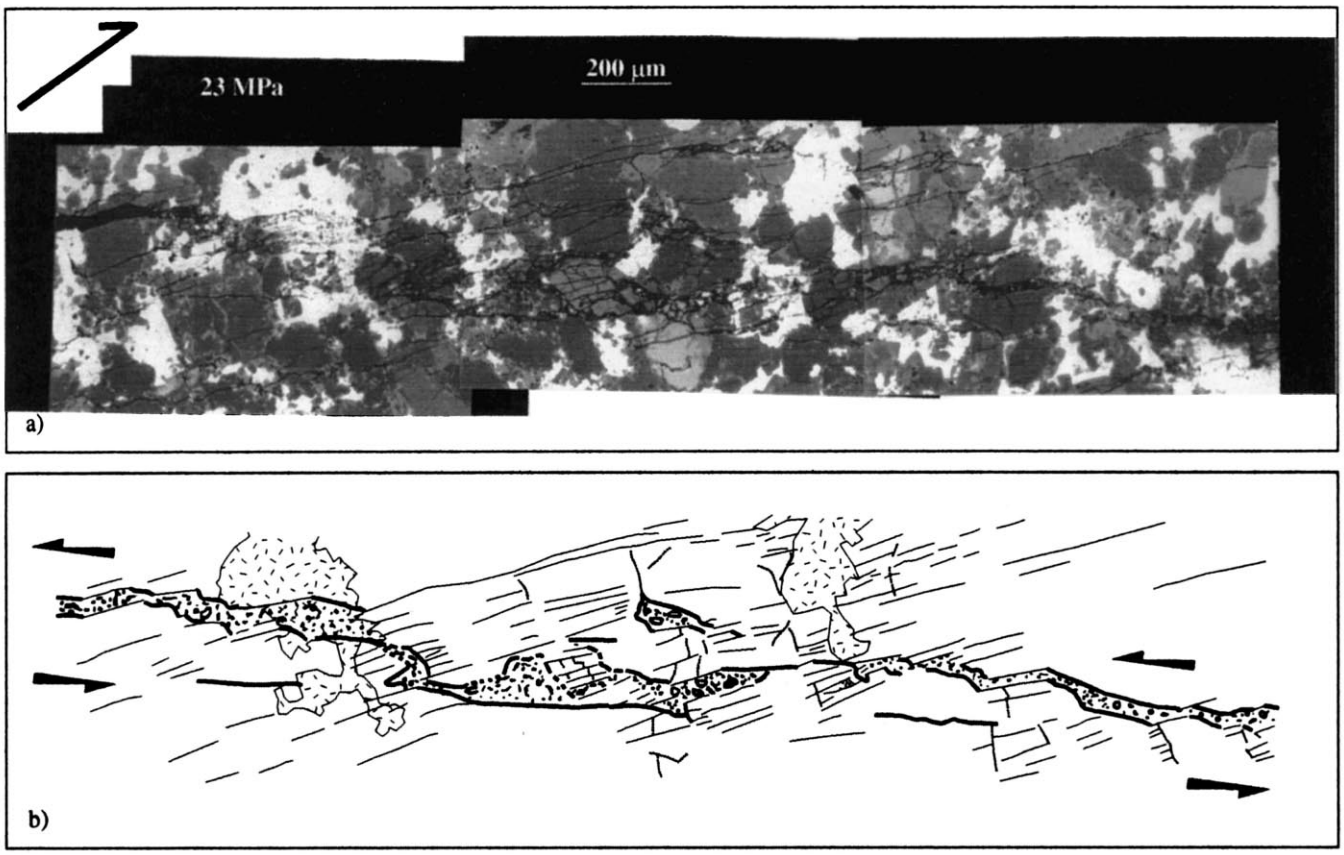

Fig. 3. Close up of a linkage zone between two high-angle microfault segment tips (located in Fig. 2). (a) Backscattered SEM montage. As in all the micrographs presented in this paper, the greyscale in the image corresponds to the mineralogy in the following way: white, calcite; light grey, orthoclase feldspar; dark grey, albite feldspar; darkest grey, quartz. (b) Interpretive drawing of the microfracture/microfault pattern.

Fig. 4. Backscattered SEM montage of part of a sample deformed by shear rupture at a normal stress of 60 MPa. Rose diagrams give the orientation statistics as measured on the scan lines (indicated in Fig. 5).

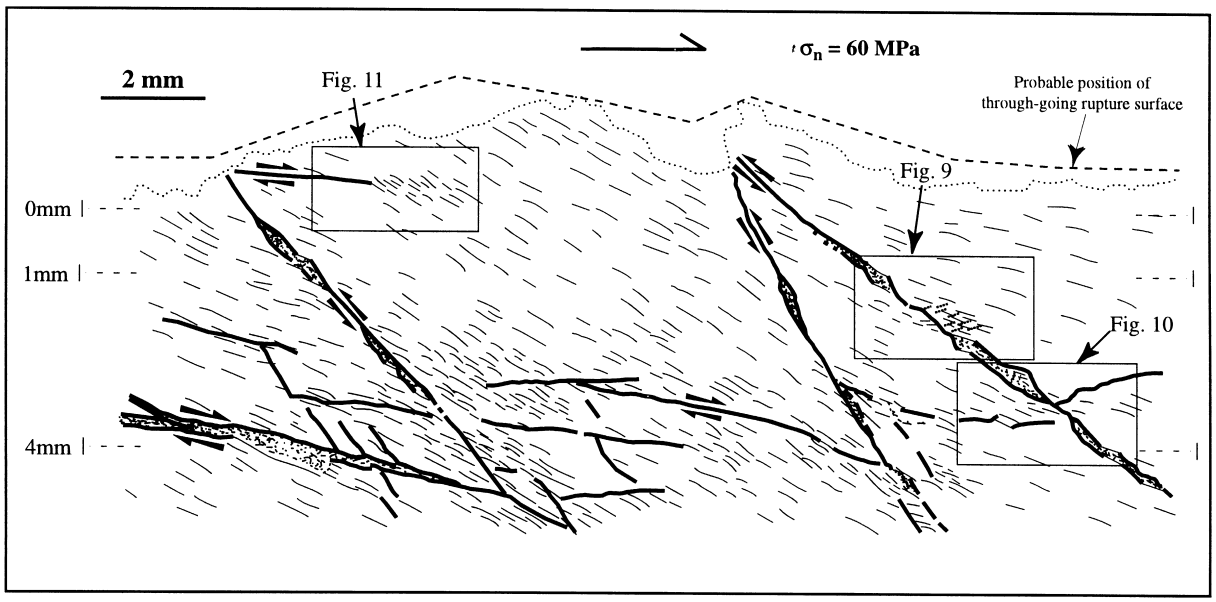

Fig. 5. Interpretive drawing of the microfracture/microfault pattern of the sample shown in Fig. 4. The scan lines marked 0 mm, 1 mm and 4 mm were used for the fracture orientation and spatial distribution statistics. The scan line markings indicate the full length of the scan lines.

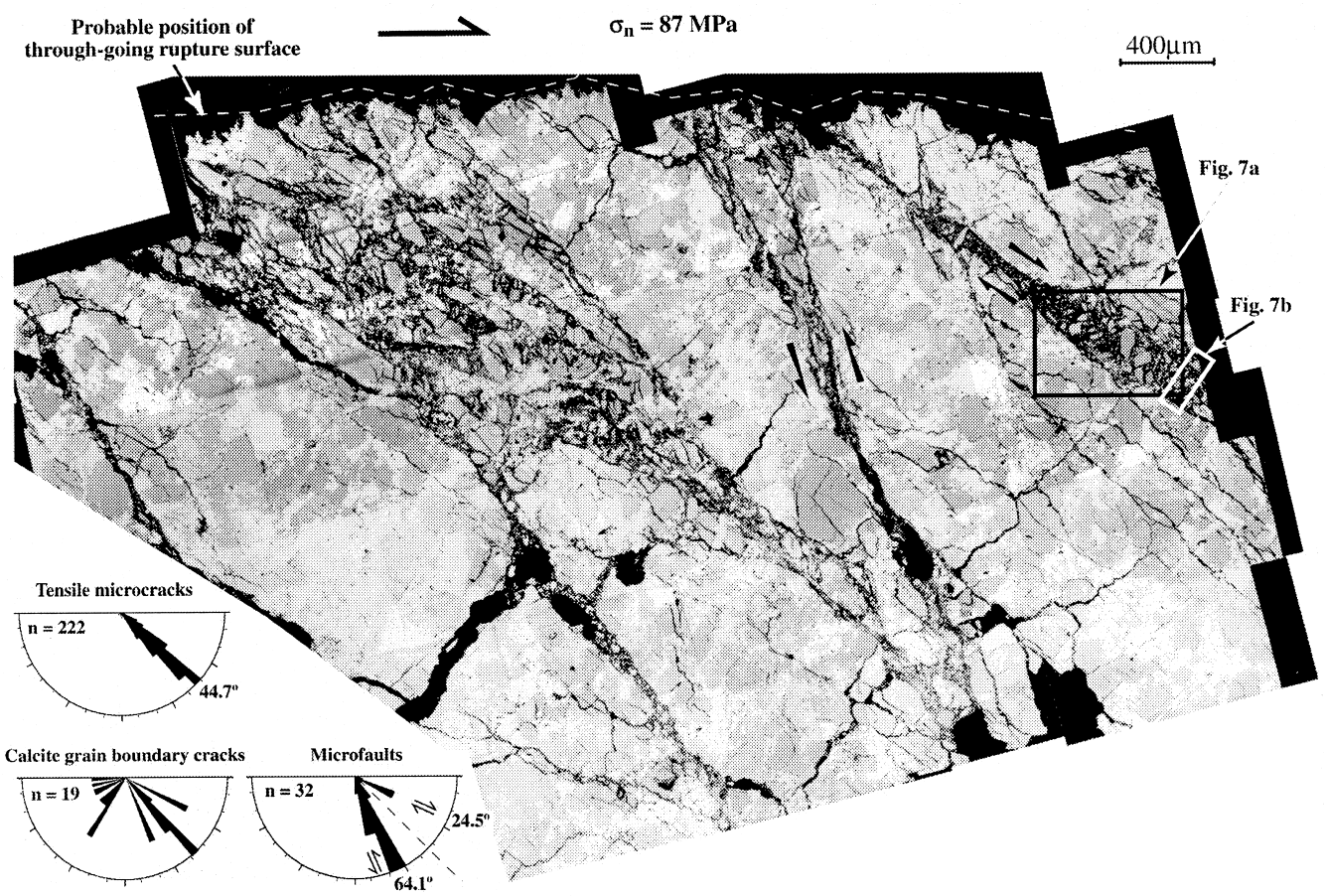

Fig. 6. Backscattered SEM montage of part of the sample deformed by shear rupture at a normal stress of 87 MPa. The statistics were collected from scan lines across the whole sample, hence correspond to a wider fracture population than that visible here. Rose diagrams give the orientation statistics.

the sample. Wall rock blocks in between the microfaults have pervasive tensile microcracks. These microcracks bisect the synthetic and antithetic microfault orientations and reflect the orientation of the local maximum compressive stress prior to failure. The dip frequency data presented in Fig. 4 show that the average tensile microcrack dip (29.1°) is greater than in the previous examples. Dip frequency data show that both classes of grain boundary crack have very variable dips but many of them are perpendicular to the rupture surface.

3.4. Samples deformed at high normal stress

A sample deformed at 87 MPa (Fig. 6) shows the largest amount of microfault damage of any of the examples presented here. Prominent microfaults exhibit a conjugate distribution as in the 60 MPa sample, but at a higher angle with respect to the overall rupture surface. The dip frequency data illustrate the orientation bimodality, but again some under-sampling of the low-angle microfaults has occurred. The microfaults in this sample contain well-developed cataclastic material, generally in ~20–200 μm thick zones. Tensile microcracks cluster closely around a 45° angle to the shear plane (average 44.7°), hence are steeper than in previous examples. Calcite grain boundary cracks either dip approximately parallel to the tensile microcracks, or dip in the opposite direction (see rose diagrams, Fig. 6).

Cataclasis has preferentially developed inside the acute angles of microfault junctions (such as the upper left part of Fig. 6), where the widest cataclasite zones are found. In such zones, many of the grains that are still nearly intact have been broken by tensile fracturing. Fracture orientations intersect the two conjugate microfault orientations that bound the brecciated zone. More detailed examples of the fragment structures in the microfaults are shown in Fig. 7. Fig. 7(a) displays evidence of both tensile grain splitting and shear displacements between grain fragments, with shear displacement evidenced by rotated grain fragments. Shear offsets of specific grain fragments can also be seen (e.g. Fig. 7b) within these microfault zones.

3.5. Summary of rupture-related fracturing at different normal stresses

Here we summarise the statistical data on rupture-related fracturing collected from the samples studied. Both the density and the average dip angle of tensile microcracks generally increase with increasing normal stress. However, the increase in measured tensile microcrack frequencies is not systematic. Data presented in Fig. 8(a) show the microcrack frequencies for each of the scan lines. In the 23 MPa sample, microcrack frequency decreases exponentially away from the rupture surface. However, in the higher normal stress cases, fracture damage is much more penetrative. Fre-

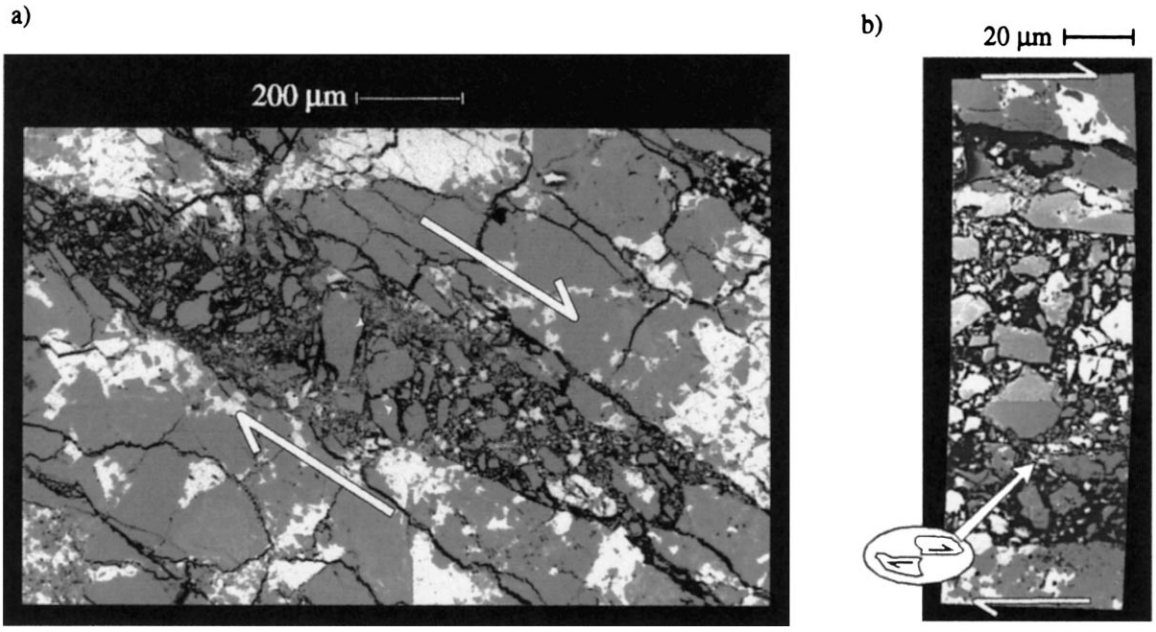

Fig. 7. (a) Close-up backscattered SEM photograph of a synthetic Riedel microfault zone, showing shear-rotation of a microclast originally incorporated into the deformation zone by tensile fracturing. See Fig. 6 for location. (b) Detailed backscattered SEM traverse showing cataclastic fragments in the microfault zone. Shear arrows and curved arrows indicate shear and opening displacements, respectively, of grain fragments. See Fig. 6 for location.

quency data measured from the sample deformed at 60 MPa suggest that microcrack density in this sample is far higher than in any of the others, even than in the 87 MPa sample. Microfault frequency data (Fig. 8b) similarly show little variation with distance from the rupture surface except in the 23 MPa case. Microfault frequencies are highest for the 60 MPa case, but almost as high for the 87 MPa case. However, it is clear from the SEM images that cataclastic zone development in the microfaults was more enhanced for the 87 MPa case. This is illustrated by the data on microfault thicknesses, presented in Fig. 8(c) as the sum of microfault zone widths per unit length of scan line, showing a systematic increase with rupture normal stress. However, for the higher normal stress cases, the increase in the sum of microfault widths per unit scan line length is accompanied by a decrease in tensile microcrack frequency (Fig. 8d).

4. Data: relationships between microcracks and microfaults

This section will describe more detailed studies of the sample ruptured at a normal stress of 60 MPa to characterise geometrical and kinematic relationships between the tensile microcracks and microfaults. The discussion section will then present mechanical interpretations of this information in the light of existing published works. The following geometrical relationships in particular will be examined:

1. The interplay between microfault geometry (such as dilational jogs and fault bends) and tensile microcracking adjacent to the microfault.
2. The relationship between microfault intersection points and tensile microcracking.
3. Tensile microcracking around microfault tips.

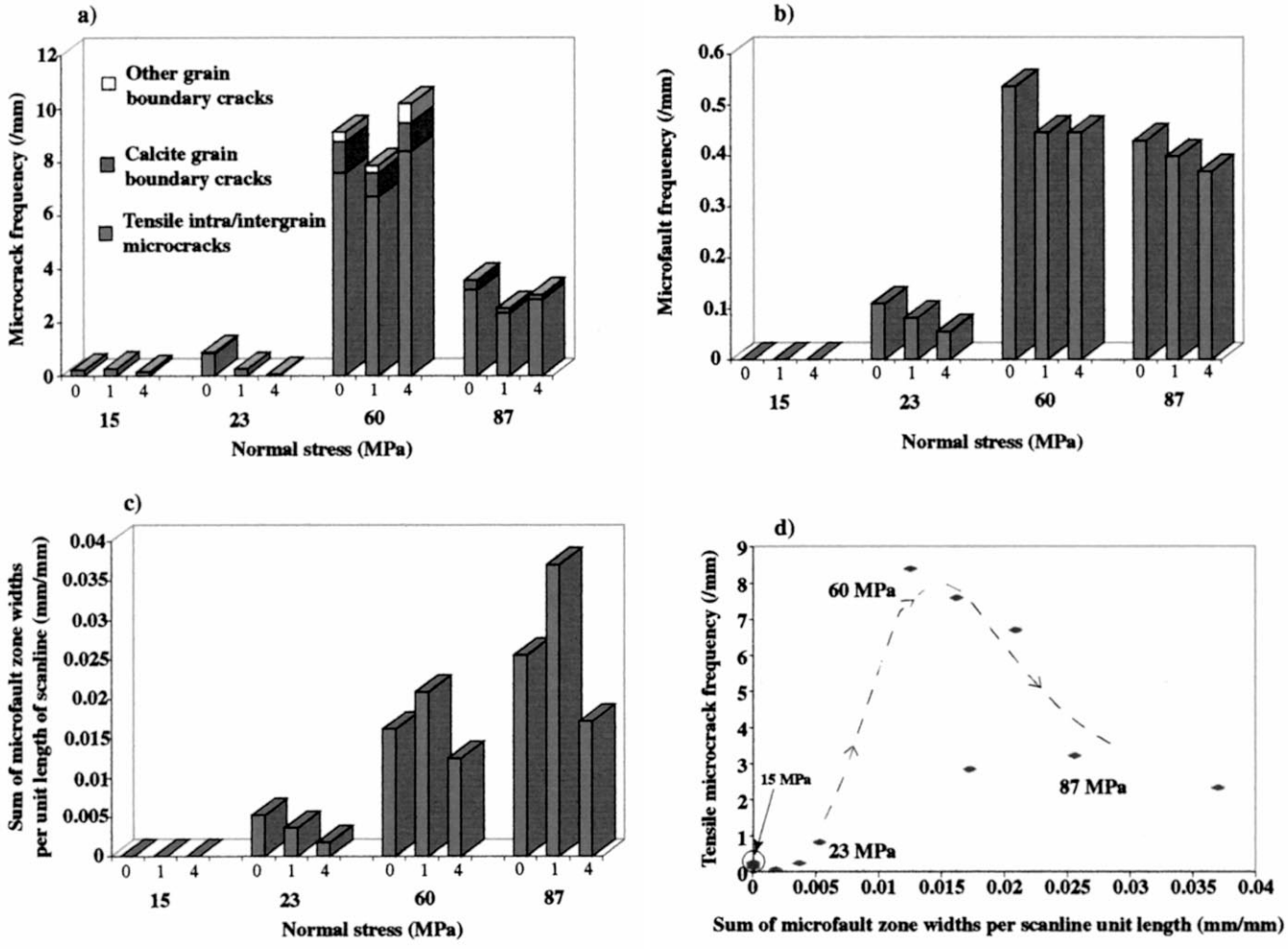

Fig. 8. Summary statistics showing variation in microcrack and microfault properties with normal stress. For (a), (b) and (c), the scan line position is also represented, with scan line distance from the rupture surface being indicated in mm, by 0, 1, and 4. (a) Microcrack frequency data; (b) microfault frequency data; (c) microfault thickness frequency data; (d) microcrack frequency versus sum of microfault thickness per mm. The dashed line in (d) suggests a dependence on normal stress and is not meant to infer a time path.

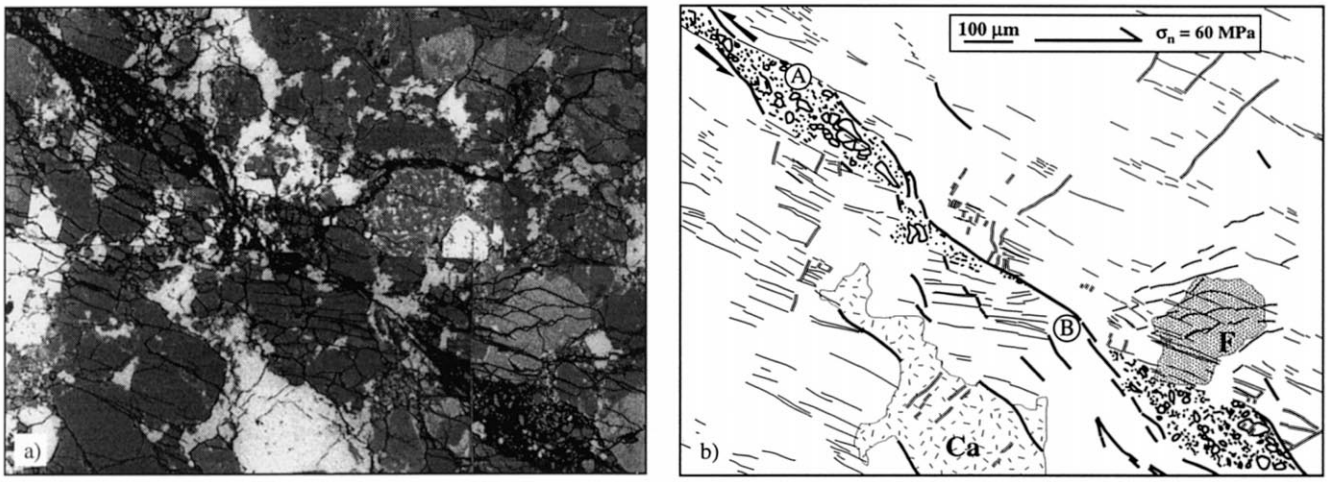

Fig. 9. Details of pull-aparts and restraining bends in an antithetic Riedel microfault zone, located on Fig. 5. (a) Backscattered SEM photograph. (b) Interpretative drawing of the microfractures and microfaults. Stippled grain labelled F denotes a potassium feldspar grain referred to in the text, flecked pattern (labelled Ca) denotes a calcite grain. Thin lines denote tensile microcracks, which can form part of the microfault wall, the remaining microfault walls being denoted by thick lines. Double thin lines represent the orientation group of cross fractures—in this example they are considered unloading cracks. Dotted lines represent a curved second generation of microcracks in a potassium feldspar grain.

4.1. Microfault jogs and bends

Fig. 9 shows an enlargement of part of Fig. 4 (see Fig. 5 for location), focusing on an antithetic microfault and its walls. Fig. 9 demonstrates how the microfaults are in places composed of micro-scale pull-aparts. The releasing edges of the pull-aparts (e.g. region A, Fig. 9b) are defined by transgranular crack edges of the same orientation as the more widely distributed tensile microcracks, and are considered to be regions where tensile microcracks have controlled microfault propagation or segment linkage. Another example of a pull-apart is displayed in Fig. 10, limited to the perthitic feldspar grain (labelled NaSpar) which is largely surrounded by calcite. Here, en échelon intragranular cracks generated within the perthitic grain prior to microfault breakthrough and pull-apart formation are likely to have been generated by a stiffness contrast with the calcite.

Fig. 9 also shows an example of a restraining bend (region B, Fig. 9), around which tensile microcrack orientations appear to have deviated from the general orientation to swing towards a fault-perpendicular orientation as they approach the fault. On the other side of the fault however, this swing in tensile microcrack orientation is not present, with two discrete sets of microcracks forming. However, here, a relatively large potassium feldspar grain (labelled 'F' in Fig. 9b)

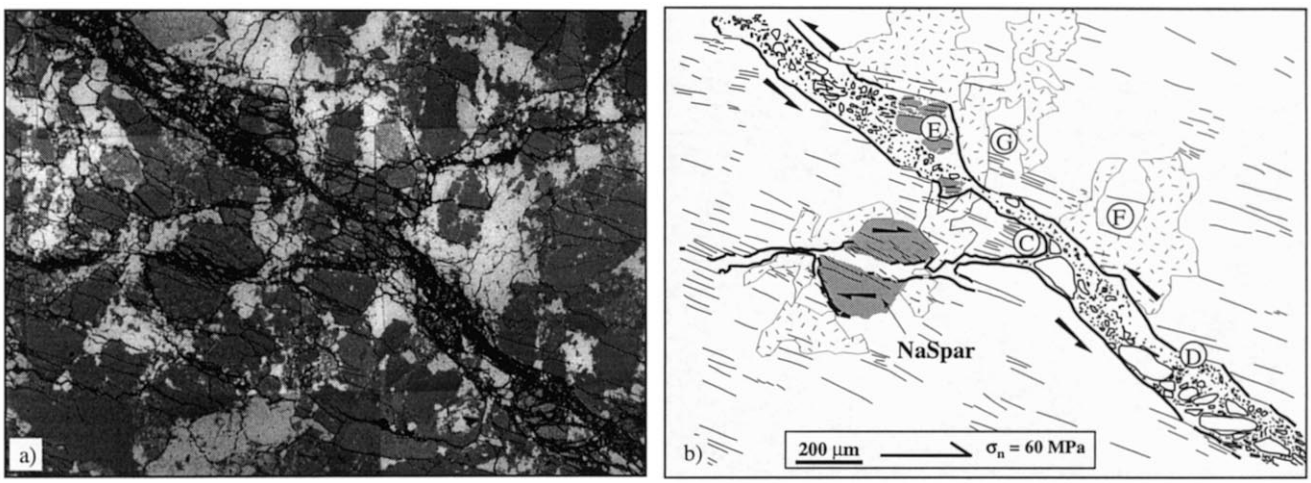

Fig. 10. Details of the tensile fracture relationships around a microfault branch point, located on Fig. 5. (a) Backscattered SEM photograph. (b) Interpretative drawing of the microfractures and microfaults. See caption to Fig. 9(b) for symbols.

dominates the area of wall rock adjacent to the restraining bend, and it is possible that cleavage played a part in controlling the evolution of tensile microcracking here (as shown by Wong, 1982).

4.2. Microfault branch and intersection zones

Fig. 10 shows an enlargement of part of Fig. 4 where two conjugate microfaults intersect. Most of the open crack in the upper right hand quarter of the image is considered to be a stress relaxation artefact based on its orientation and appearance. It is not drawn on the interpretative fracture map of Fig. 10(b). Tensile microcracks of the 'general' orientation are observed away from the microfaults, but in Fig. 10 they increase their density in the acute angle zone of the microfault intersection (region C in Fig. 10b). Nearly all the other examples of microfaults in Fig. 4 also show this same phenomenon. In these cases, tensile microcracks have become so dense that fragmentation has occurred locally, generating cataclasite (e.g. region C, Fig. 10b). Another example of localised cataclasis is seen in region E in Fig. 10. Here, albite fragments have been split by tensile microcracks in a zone of microfault widening, with the microfault boundary following a calcite/feldspar grain boundary. This relationship suggests a mineralogical control on cataclasis, investigated further in the discussion section on the control of mineralogy on tensile microcracking and microfault development. Fracture densities are also seen to be anomalously low in several regions of Fig. 10. Many of these regions, such as regions F and G in Fig. 10(b) are adjacent to regions of high microcrack densities close to the intersection zone. In these cases the fracture densities are anomalously low either in calcite grains, or in albite (region F) or quartz (region G) grains continuously surrounded on at least three sides by calcite.

4.3. Microfault tip zones

Fig. 11(a) shows a third enlargement of part of Fig. 4, showing the tip zone of a synthetic microfault. A region of relatively long, open, well-developed tensile transgranular en échelon microcracks (of the same orientation as the pervasive tensile microcracking) is present adjacent to the tip of the microfault. This region is considered to be a fracture process zone to the microfault. A concentration of tensile cracks is also observed in the microfault walls adjacent to the walls of the microfault where it is already developed, suggesting the presence of a 'wake zone' of palaeo-process zone microcracks. However, the present process zone is defined by fractures that are much longer than the microcracks in the wake zone. In Fig. 11(a), a group of secondary tensile microcracks that formed perpendicular to the general tensile microcrack orientation are observed in the immediate area around the microfault tip, and their distribution is highlighted in Fig. 11(b). They connect (or 'cross-link') successive parallel en échelon fractures in a zone labelled IB (incipient breakdown zone) on Fig. 11(b). Another zone of these secondary cross-linking microcracks is observed immediately adjacent to the edge of the microfault (region H, Fig. 11b). This zone is probably responsible for helping wall rock regions of tensile microcracking to become cataclastic fragments in the microfault zone (see also Fig. 10, region E), as discussed in the following section.

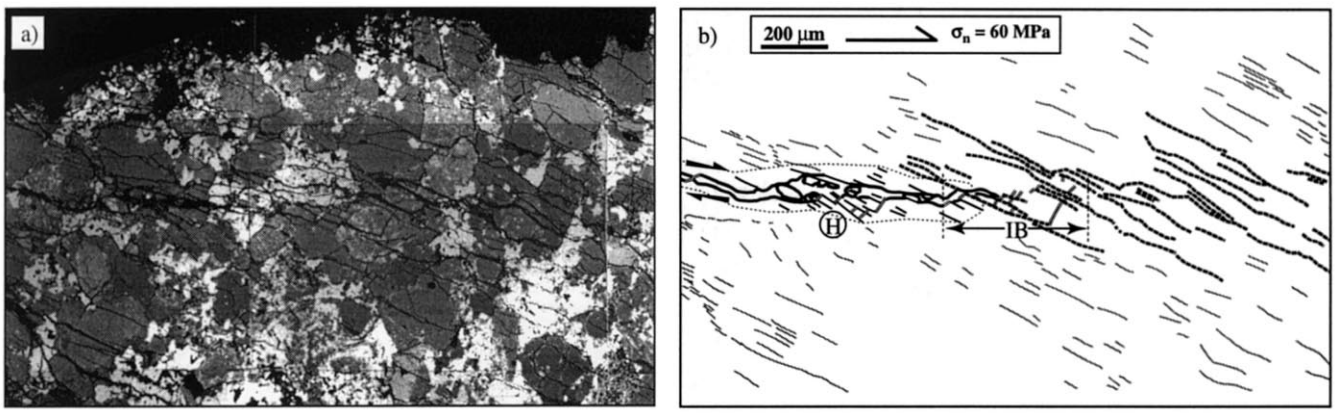

Fig. 11. Details of the tip zone of a synthetic Riedel microfault, located on Fig. 5. (a) Backscattered SEM photograph. (b) Interpretative drawing of the microfractures and microfaults. See caption to Fig. 9(b) for symbols, but in addition, thick dashed lines denote transgranular tensile microcracks in the process zone, thin dotted lines mark an estimation of the microfault wake zone limits, and IB denotes the incipient breakdown zone of the microfault tip (see text for explanation).

5. Discussion: fault/crack micromechanics

5.1. Relationship between microcracking and microfault development

Except for the 15 MPa sample, tensile intra- and transgranular microcracks are observed in all the samples. These tensile microcracks are analogous to those previously described from triaxial compressive tests. For triaxial tests, recent works (e.g. Reches and Lockner, 1994) present microscopic studies and acoustic emission data at various stages of pre-rupture strain. These works have described the presence of initially randomly distributed cracks forming parallel to the direction of maximum compression. Microfault initiation is suggested to occur by the en échelon linkage of a few of these cracks, and stress concentrations at the microfault tip cause more tensile cracking in a specific moving zone as the microfault tip propagates. Understanding the controls on these tensile crack/microfault interactions is therefore crucial to understanding fault micromechanics.

5.1.1. Microfault propagation

Fault propagation by a mechanism of en échelon tensile crack linkage has been proposed in the past from field evidence (e.g. Etchecopar et al., 1986; McGrath and Davison, 1995) and from experimental evidence (e.g. Petit and Barquins, 1988; Lockner et al., 1991). However, the way in which en échelon cracks actually connect to each other has been little addressed. For mode III fault propagation, Cox and Scholz (1988) suggest that a high enough density of tip zone fractures will, with a certain orientation variability, lead to their connection and to process zone failure. However Moore and Lockner (1995) suggested that the buckling of the intact zones (which we call 'beams') between parallel en échelon process zone fractures could cause microfault tip propagation. We show in Fig. 11 a microfault tip process zone, which has a set of very short microcracks (region IB, Fig. 11b) perpendicular to the general direction of en échelon transgranular microcracks. Their generation allows connection of successive parallel en échelon fractures by cross-linking. Because they form in that part of the process zone immediately at and ahead of the microfault termination, this cross-linking allows an increase in length of the through-going microfault surface, hence propagation. The mechanism for generating such short tensile microcracks is suggested to be the slight bending of the beams between the en échelon fractures induced during fault tip folding (Fig. 12). Such folding, although very subtle because it is elastic and therefore not detectable in Fig. 11(a), could create sufficient bending stresses in the beam zones to generate tensile microcracking within the beams [Fig. 12, stage (i)]. This may quickly evolve when the zone accommodates some shear displacement, with total breakdown of the beams by fragmentation [Fig. 12, stages (ii) and (iii)], and a continuous propagation of the fault tip.

Continued propagation of the microfault tip should leave zones of tensile en échelon microcracks in its wake either side of the microfault. Such zones may be termed 'palaeo-process zones' or 'wake zones' (e.g. Cox and Scholz, 1988), and such zones have recently been suggested by detailed observations of microfrac-

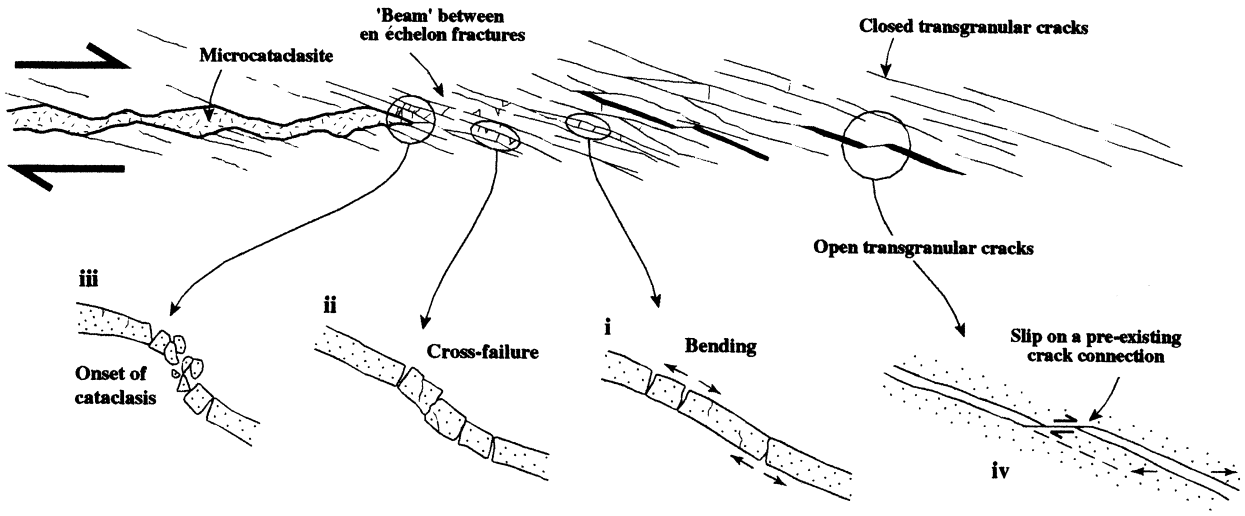

Fig. 12. Sketch model for the propagation of a microfault, showing the micromechanisms within the incipient breakdown zone at the immediate tip of a microfault. The presence of calcite is not taken into account. Only transgranular cracks are shown. (i), (ii) and (iii) Different steps of collapse of the beams limited by two transgranular cracks. Collapse is initiated by tensile cracking due to stresses linked to beam bending during the shear movement (fault tip folding). (iv) The mechanism for transgranular crack opening.

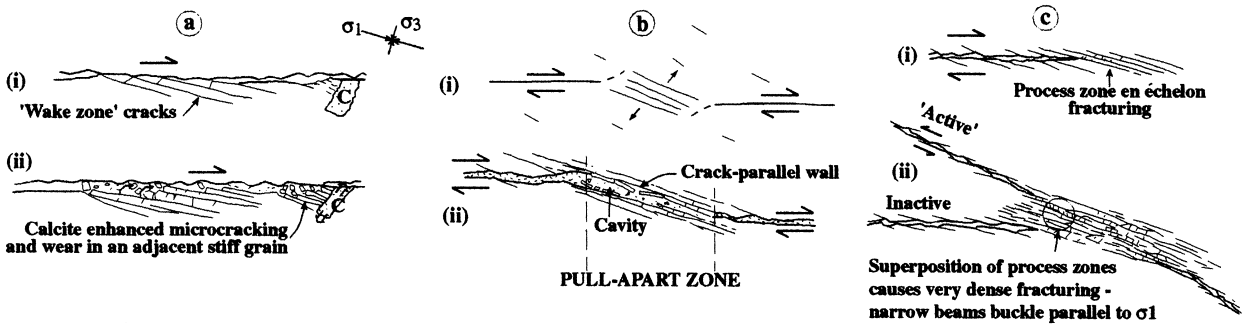

Fig. 13. Summary of the different micromechanisms contributing to cataclasite generation in the microfaults. (a) Wear of beams oblique to the walls of microfaults with dilatancy, fragmentation and tilting of beams. (b) Axial splitting enhancement and collapse along pull-apart walls. Splitting is linked to the deconfining effect of the aperture. (c) Intense microfracturing linked to stress concentration at microfault intersections. In the illustrated case, collapse of beams is facilitated by bending induced by fault-tip folding on the latest formed microfault (similar to the mechanism presented in Fig. 12).

ture densities adjacent to natural metre-scale faults (Vermilye and Scholz, 1998). In Fig. 11 tensile cracks are observed adjacent to the microfault. However, the present process zone is defined by transgranular tensile fractures that are much longer than the microcracks in the wake zone. This is interpreted to reflect a rapid decrease in the differential stress during a late stage of the loading cycle. In this situation, the process-zone cannot continue to migrate, so that those transgranular, en échelon cracks stay in the process-zone much longer, and can grow until the maximum compressive stress becomes too low, after total rupturing of the sample.

5.1.2. Microfault bends and tensile microcracking

Whilst specific geometric features of microfaults are controlled by tensile microcracks, conversely, tensile microcracking can occur by processes related to microfault slip. Microfault pull-aparts are defined by crack walls at low angles with respect to the microfault. They have formed in zones of concentrated tensile microcracking [e.g. Figs. 9 (region A) and 10 (region D and E)] so that a proportion of the microfault surfaces are defined by pre-existing tensile microcrack surfaces. This is locally consistent with descriptions of 'sawtooth' geometries of fault walls, such as described by Moore and Lockner (1995). In these pull-apart zones some of the intense tensile microcracking may occur by splitting related to local deconfinement as the pull-apart opens during microfault slip. Furthermore, Fig. 9 also illustrates an example of a restraining bend in the microfault geometry (region B). The curving microcrack geometry on the left hand side of the microfault here is interpreted as reflecting the stress perturbation encountered at such restraining bends, and is similar to outcrop observations of the same phenomenon (e.g. Rawnsley et al., 1992; Petit and Mattauer, 1995). On the other side of the microfault, Fig. 9 shows two distinct microcrack generations, which we interpret as reflecting a control of potassium feldspar cleavage on microcrack evolution in a rotating stress field during restraining-bend evolution. The first generation cracks are straight and perhaps parallel to one of the cleavages, whilst the second generation are formed as the stress trajectories are rotated at the restraining bend, the curving-to-perpendicular style indicating the influence of the cleavage parallel cracks acting as free surfaces. Hence these pull-aparts and restraining bends illustrate the continued interdependence between tensile microcracking and microfault development during continued deformation, not necessarily related to microfault tip propagation.

5.1.3. Cataclasite generation

In the moderate and high normal stress experiments, cataclastic material was generated in the microfault zones. The data presented in Section 3 show that final microcrack and microfault frequencies are inter-related, depending on rupture normal stress, as the overall rupture damage increases with increasing normal stress. However, in order to improve our understanding of the micromechanisms of fault development, we need to address the following question. Does the increase in microfault density within a sample correspond to a larger tensile microcrack density, or could microfault localisation and development occur at the expense of pre-existing microcracks or further microcrack development? Whilst generally a correlation exists between microfault and tensile microcrack frequencies (as seen by comparing Figs. 2, 4 and 6), the 60 and 87 MPa cases have very similar microfault frequencies despite quite different tensile microcrack frequencies, suggesting an upper limit exists to the density of microfaults (Fig. 8b). Fig. 8(d) shows that the higher normal stress cases have an inverse correlation between the sum of microfault zone widths and tensile microcrack frequency. These data suggest that after an upper limit to the density of microfaults has

been reached, further deformation is by microfault zone widening using the pre-existing tensile microcracks, and effectively 'destroying'[1] them in the process (e.g. Fig. 7a). Whilst the tensile, transgranular microcracks have clearly caused initial breakage of the wall rock, friction between microfault fragments and wall rock during fault slip can have an abrasive effect leading to ploughing of more material weakened by the initial tensile cracking (Fig. 13a).

Fault wall cataclasis can occur during pull-apart formation (Fig. 13b). Intense tensile microcracking evolving towards beam collapse within the opening pull-apart is enhanced by local tensile stress along the σ_3 direction due to the deconfining effect of the opening. This effect could be dramatically enhanced by the intense initial fracturing which may result from the interaction of two parallel microfaults propagating towards each other (Fig. 13bi).

One final mechanism for cataclasis is damage by fault intersection. In the highest normal stress case, relatively wide zones of immature cataclasite form by collapse of the beams in between dense tensile microcracks. These zones are observed in the acute angle regions of microfault (synthetic and antithetic Riedel) intersections (e.g. Figs. 4 and 10), such as in Fig. 6 next to the through-going main rupture surface. In such cases, the tensile transgranular microcracks become so dense and closely spaced that the beams in between are very narrow and buckle more easily (Fig. 13c). This buckling is encouraged by higher differential stresses.

5.2. Control of mineralogy on tensile microcracking and microfault development

Many of the images presented in this study (e.g. Figs. 9 and 10) show examples of how compliant calcite grains have lower crack densities than adjacent, highly fractured, stiffer grains. A comparable situation was attributed by Tapponnier and Brace (1976) and Dey and Wang (1981) to the contrast in stiffness between two adjacent grains leading to the cracking in the stiffer grain. Fig. 14 presents generalised situations of how stiff/compliant grain contrasts result in microcracking in the stiffer grain. A single edge (oriented perpendicular to the direction of maximum compressive stress) of a stiff grain compressed against a compliant calcite grain leads to wedge cracking in the stiff grain (Fig. 14a), parallel to the maximum compressive stress direction (Tapponnier and Brace, 1976). Region E in Fig. 10 is an example of this. Similarly, if a second edge opposite to this first edge is also adjacent to calcite, axial splitting may occur (Fig. 14b). If the calcite is adjacent to a stiff grain on opposite diagonals, then en échelon tensile microcracking and 'pull-apart' splitting of the stiff grain may occur (Fig. 14c) and this is observed in the perthitic feldspar grain labelled 'NaSpar' in Fig. 10(b). Finally, calcite can have a shielding effect if it totally, or nearly totally, surrounds a stiff grain. Examples approaching this situation are seen in Fig. 10 (regions F and G, Fig. 10b). Here, deformation may be accommodated by plastic mechanisms within the calcite, so that the deviatoric stress within the stiff grain remains low (Fig. 14d).

5.3. Control of normal stress on wall rock fracturing and hydrodynamic properties

There is a clear increase in both the amount of 'fracture damage' and the general dip of the fractures with increasing normal stress (Figs. 2, 4, 6 and Table 1). This corroborates much relatively early work, mainly on triaxial testing, summarised by Kranz (1983), for example, who states that the number and size of these microcracks is greater for samples deformed at higher pressures. Fig. 8 shows that a clear increase in the width of the microfault cataclasite zones was observed with increasing normal stress. The high proportion of space in these cataclastic microfault zones (e.g. Fig. 7) suggests that wall rock fracture porosity should be

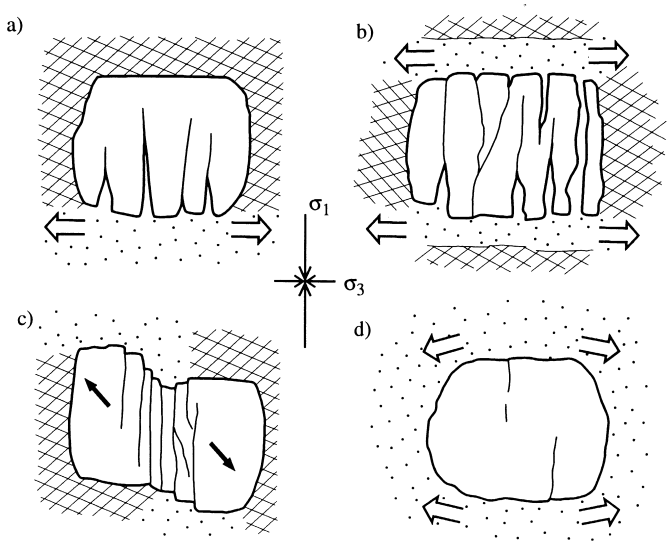

Fig. 14. Effect of the presence of easily deformed calcite grains (dots) on the development of intragranular cracks in a stiff (quartz or feldspar) grain. Cross-hatching indicates surrounding stiff minerals. Small arrows indicate extension in calcite crystals. Local main principal stress is vertical. (a) Wedge cracking (as proposed by Tapponnier and Brace, 1976). (b) Axial splitting. (c) En échelon splitting. (d) Limited splitting of an isolated stiff grain.

[1] The microcrack surfaces will still exist, but they will be defining grain fragment surfaces within the cataclastic zone. Hence they will not be individual tensile cracks any more, and will not be counted as such.

Table 2
Dependency of rupture zone mechanical and hydrodynamical properties on rupture normal stress—↑ denotes positive dependency, ↓ denotes negative dependency

	Through-going rupture surface	Wall rock damage zone
Fracture density	↑	↑
Cataclastic grain size reduction	↑	↑
Dilatancy	↓	↑
Fracture porosity	↓	↑
Permeability coefficient	↓	↑
Storativity	↑	

much more enhanced by rupture at high normal stresses than at low normal stresses. Also, the angle between synthetic and antithetic microfaults and the microfault and tensile microcrack densities and penetration distance into the wall rock all increased with increasing normal stress. This suggests that wall rock fracture permeabilities, in all directions, should also be much more enhanced by rupture at high normal stress than at low normal stress. The converse should be true for permeability at the rupture surface itself, at least in the *y*-direction (perpendicular to the rupture zone sections presented in Fig. 1b and Figs. 2–7). The formation of macroscopic dilational jogs at low normal stress (Petit, 1988 and Fig. 1b) would highly enhance permeability at the rupture surface in the *y*-direction.

This has gross implications for the storativity of the system as a whole. The importance of fracture damage zones around faults for fluid storage has recently been discussed by Seront et al. (1998) in the light of evidence from seismogenic normal fault zones. In real terms, the storativity will depend on the ability of the system to hold the fluid in 'dead end' fracture volume, with the minimum ability to drain via the actual through-going rupture surface. Clearly, our examples of rupture at higher normal stresses (60 and 87 MPa) match these criteria better than the examples of rupture at low normal stresses (15 and 23 MPa). These qualitative estimations of the reliance of hydrodynamic parameters on normal stress during rupture are summarised in Table 2.

Our observations from low-porosity sandstone samples differ from those on dilatancy for triaxial failure at different confining pressures for the case of high porosity sandstone (Gowd and Rummel, 1980) where differential volumetric strain for the samples as a whole was much higher in the lowest confining pressure cases. However, their bulk sample strain measurements do not separate the dilatancy of through-going rupture surface from that of the wall rock fracture network. In their high confining pressure tests for example, pressure-enhanced compaction in the fault zones is likely to become an important factor. Furthermore, compaction in the fault zones is likely to be enhanced much more for high porosity sandstones at higher normal stresses, because of the high proportion of void space available to be lost. In our case of very low porosity sandstones however, compaction is much more difficult to achieve. Our findings also provide an interesting contrast with the likely permeability of a fault zone after rupture. Studies of permeability evolution during continued shear of experimentally deformed gouge show that deformation at high normal stress most reduces fault rock permeability (e.g. Zoback and Byerlee, 1976). Our findings here on wall rock fracturing due to the initial rupture phase of deformation compliment these studies by contributing new information which may be incorporated with existing data towards an overall model of fault and damage zone permeability and its evolution with time. Current ideas (e.g. Evans et al., 1997) emphasise the importance of wall rock ('damage zone') fracturing in fault permeability models, and the present work demonstrates the role of normal stress during the rupture phase.

6. Conclusions

6.1. Fault/fracture relationships

Experimental shear rupture of low porosity sandstone shows an increase in wall rock pre- to syn-failure cataclastic damage intensity and penetration around the rupture zone with increasing rupture normal stress in the range 15–87 MPa (Table 1). Fracture damage in the walls to the rupture surfaces consists of distributed tensile microcracks and microfaults that contain cataclastic material of varying grain size. Fracture micromapping reveals features similar to larger scale fault zones, such as fault process zones and dilational pull-aparts (e.g. Fig. 4). Detailed SEM imaging of microfaults has evidenced the reliance on 'general' tensile wall rock microcracking for propagation and cataclasis whilst at the same time controlling sites of stress concentration at fault tips, intersections and relay zones (Figs. 9–11). Microfault density achieved an upper

limit, beyond which further damage occurred by microfault widening, making use of, and destroying, pre-existing tensile microcracks. Microfault cataclasite was generated from wall rock weakened by tensile microcracking by friction during fault slip, releasing fragments that were rotated into the microfault zones (Fig. 13). Mineralogy and grain structure exert strong controls on tensile microcracking and microfault development, the most important being the compliancy of calcite which induces tensile cracking in neighbouring stiffer grains, or shields stiffer grains completely from deformation (Fig. 14).

6.2. Damage zone hydrodynamics

Microfault density, range of orientations, connectivity, penetration into the wall rock, and porous cataclastic zone widths are all increased at increased rupture normal stress. Because of the open fracture space associated with these structures (e.g. Fig. 7), these results suggest that an increased wall rock fracture porosity and permeability is achieved due to shear rupture fracturing with increasing normal stress in these experiments. Implications for fracture volume also suggest that the storativity of the system will increase dramatically with rupture normal stress over our experimental normal stress range (Table 2).

6.3. Microfault propagation

New evidence on fracture micromechanics shows the importance not only of en échelon fracture arrays in Mode II microfault tip propagation, but also of microcracks cross-linking such en-échelon fractures in an incipient breakdown zone (Fig. 11). The cross-linking microcracks are considered to form due to bending stresses in the beams between the en échelon fractures (Fig. 12). A complete physical understanding of microfault propagation in low porosity rocks must therefore consider the mechanics of beam bending and cross-fracturing. Beam cross-fracturing is crucial because it is the final process which provides a connected fracture pathway necessary for the fault to be propagating, and could therefore be a factor in controlling the shear strength of the rock.

Acknowledgements

The thin section work and interpretations were carried out when the first author was in receipt of an Elf Aquitaine post-doctoral research grant, which is gratefully acknowledged. Feedback from Phillippe Gouze greatly improved the hydrodynamics aspects. The first author would also like to thank M. Gris and M. Rossi for assistance with the scanning electron microscope, and Anne Delplanque for help with drafting the figures. The manuscript was greatly improved by suggestions from Diane Moore and Richard Lisle.

References

Brace, W.F., Bombolakis, E.G., 1963. A note on brittle crack growth in compression. Journal of Geophysical Research 68, 3709–3713.

Brace, W.F., Paulding, J.B.W., Scholz, C., 1966. Dilatancy in the fracture of crystalline rocks. Journal of Geophysical Research 71, 3939–3953.

Cox, S.J.D., Scholz, C.H., 1988. On the formation and growth of faults: an experimental study. Journal of Structural Geology 10, 413–430.

Dey, T.N., Wang, C.-Y., 1981. Some mechanisms of microcrack growth and interaction in compressive rock failure. International Journal of Rock Mechanics, Mining Sciences and Geomechanics abstracts 18, 199–209.

Dunn, D.E., LaFountain, L.J., Jackson, R.E., 1973. Porosity dependence and mechanism of brittle fracture in sandstones. Journal of Geophysical Research 78, 2403–2417.

Etchecopar, A., Granier, T., Larroque, J.M., 1986. Origin of en échelon cracks—propagation of faults. Comptes Rendus de l'Academie des Sciences serie II 302, 479–484.

Evans, J.P., Forster, C.B., Goddard, J.V., 1997. Permeability of fault-related rocks, and implications for hydraulic structure of fault zones. Journal of Structural Geology 19, 1393–1404.

Gallagher Jr., J.J., Friedman, M., Handin, J., Sowers, G.M., 1974. Experimental studies relating to microfracture in sandstone. Tectonophysics 21, 203–247.

Gowd, T.N., Rummel, F., 1980. Effect of confining pressure on the fracture behaviour of a porous rock. International Journal of Rock Mechanics, Mining Sciences and Geomechanics abstracts 17, 225–229.

Granier, T., 1985. Origin, damping, and pattern of development of faults in granite. Tectonics 4, 721–737.

Hallbauer, D.K., Wagner, H., Cook, N.G.W., 1973. Some observations concerning the microscopic and mechanical behaviour of quartzite in stiff triaxial compression tests. International Journal of Rock Mechanics, Mining Sciences and Geomechanics abstracts 10, 713–726.

Horii, H., Nemat-Nasser, S., 1985. Compression induced microcrack growth in brittle solids: Axial splitting and shear failure. Journal of Geophysical Research 90, 3105–3125.

Kranz, R.L., 1983. Microcracks in rocks: a review. Tectonophysics 100, 449–480.

Lockner, D.A., Byerlee, J.D., Kuksenko, V., Ponomarev, A., Sidorin, A., 1991. Quasi-static fault growth and shear fracture energy in granite. Nature 350, 39–42.

Lockner, D.A., Byerlee, J.D., Kuksenko, V., Ponomarev, A., Sidorin, A., 1992. Observations of quasi-static fault growth from acoustic emissions. In: Evans, B., Wong, T.-F. (Eds.), Fault Mechanics and Transport Properties of Rocks. Academic Press, San Diego, pp. 3–31.

McGrath, A.G., Davison, I., 1995. Damage zone geometry around fault tips. Journal of Structural Geology 17, 1011–1024.

Moore, D.E., Lockner, D.A., 1995. The role of microcracking in shear-fracture propagation in granite. Journal of Structural Geology 17, 95–114.

Paterson, M.S., 1978. Experimental rock deformation—the brittle field. Springer-Verlag, Berlin.

Peng, S., Johnson, A.M., 1972. Crack growth and faulting in cylindrical specimens of Chelmsford granite. International Journal of Rock Mechanics, Mining Sciences and Geomechanics abstracts 9, 37–86.

Petit, J.-P., 1988. Normal stress dependent rupture morphology in direct shear tests on sandstone with applications to some natural fault surface features. International Journal of Rock Mechanics, Mining Sciences and Geomechanics abstracts 25, 411–419.

Petit, J.-P., Barquins, M., 1988. Can natural faults propagate under mode II conditions? Tectonics 7, 1243–1256.

Petit, J.-P., Barquins, M., 1990. Fault propagation in mode II conditions: Comparison between experimental and mathematical models, applications to natural features. In: Rossmanith, H.P. (Ed.), Mechanics of Jointed and Faulted Rock. A.A. Balkama, Rotterdam, pp. 213–220.

Petit, J.-P., Mattauer, M., 1995. Palaeostress superimposition deduced from mesoscale structures in limestone: the Matelles exposure, Languedoc, France. Journal of Structural Geology 17, 245–256.

Rawnsley, K.D., Rives, T., Petit, J.-P., Hencher, S.R., Lumsden, A.C., 1992. Joint development in perturbed stress fields near faults. Journal of Structural Geology 14, 939–951.

Reches, Z., Lockner, D.A., 1994. Nucleation and growth of faults in brittle rocks. Journal of Geophysical Research 99, 18159–18173.

Scholz, C.H., 1968. Microfracturing and the inelastic deformation of rock in compression. Journal of Geophysical Research 73, 1417–1432.

Seront, B., Wong, T.-F., Caine, J.S., Forster, C.B., Bruhn, R.L., Fredrich, J.T., 1998. Laboratory characterization of hydrodynamical properties of a seismogenic normal fault system. Journal of Structural Geology 20, 865–881.

Tapponnier, P., Brace, W.F., 1976. Development of stress-induced microcracks in Westerly Granite. International Journal of Rock Mechanics, Mining Sciences and Geomechanics abstracts 13, 103–112.

Vermilye, J.M., Scholz, C.H., 1998. The process zone: A microstructural view of fault growth. Journal of Geophysical Research 103, 12223–12237.

Wong, T.-F., 1982. Micromechanics of faulting in Westerly granite. International Journal of Rock Mechanics, Mining Sciences and Geomechanics abstracts 19, 49–64.

Zoback, M.D., Byerlee, J.D., 1976. A note on the deformational behavior and permeability of crushed granite. International Journal of Rock Mechanics, Mining Sciences and Geomechanics abstracts 13, 291–294.